IEEE Access
Multidisciplinary | Rapid Review | Open Access Journal

Received May 15, 2021, accepted June 13, 2021, date of publication June 17, 2021, date of current version June 25, 2021.

Digital Object Identifier 10.1109/ACCESS.2021.3090180

Evaluating the Maximum Directional Kinematic Capability of a Redundant Manipulator Based on Allowable Velocity and Force

JONG HO KIM[1], YOUNG JUNE SHIN[2], AND IN GWUN JANG[1], (Member, IEEE)
[1]Cho Chun Shik Graduate School of Green Transportation, Korea Advanced Institute of Science and Technology (KAIST), Daejeon 34051, South Korea
[2]Agency for Defense Development (ADD), Daejeon 34060, South Korea

Corresponding author: In Gwun Jang (igjang@kaist.edu)

This work was supported by the National Research Foundation of South Korea (NRF) grant through the Korea Government (MSIT) under Grant 2021R1A2C200986011.

ABSTRACT In this study, a new concept of allowable velocity and force is proposed to precisely evaluate the maximum directional kinematic capability of a redundant manipulator. For a general redundant manipulator, an optimization problem is formulated to determine the maximum achievable velocity and force projected along the base direction at any target position in the workspace. This provides quantitative information on allowable (i.e., maximum directional) velocity and force to be precisely visualized in 2D and 3D complicated shapes, which conventional manipulability ellipsoid cannot provide. As application examples, allowable velocity and force are evaluated for a distributed actuation mechanism (DAM)-based three-link planar manipulator, 3RRR planar parallel manipulator, and the UR5 robot (a spatial manipulator with 6 degrees of freedom). The simulation and experimental results validate that the proposed method can precisely determine allowable velocity and force, thereby contributing to planning the optimal operation for a given task.

INDEX TERMS Allowable velocity, allowable force, robot kinematics, redundant manipulator, gradient-based optimization.

I. INTRODUCTION

Demand for complicated manipulation has expanded into diverse areas such as service, military, and surgical/health applications. Manipulators are often required not only to have high performance for a specific measure in one situation, but also to enhance a different type of performance measure in another situation. For example, high-speed and large-force operation with a limited power source is an ever-challenging issue. Thus, it is important to precisely evaluate the maximum capability of a manipulator in terms of velocity and force. The most widely used method to evaluate such capabilities is to obtain the manipulability ellipsoid [1], which can visualize the performance of an end-effector [2]. Similarly, the manipulability measure can be used as a scalar index which is derived from the volume of the manipulability ellipsoid [3]. Chiu [4] also proposed a performance index that uses velocity and force ellipsoids to measure the compatibility of a generalized manipulator task. However, because the maximum speed in the joint space is assumed to be the same unit value (i.e., a hypersphere), the results of performance analysis are generally underestimated [5]. Although the concept of force polytope and scaled force ellipsoid were subsequently proposed [6], the maximum performance could not be precisely evaluated due to the aforementioned limited utilization of resources in the joint space. Therefore, a new method needs to be developed to provide reliable information on the maximum capability of a general manipulator.

Actuation mechanism at the assembly level can also significantly affect the manipulation performance [7]–[10]. Because a kinematically redundant mechanism has a higher number of actuators than degrees of freedom (DOFs), a redundant actuation mechanism can be used to execute an additional task (e.g., obstacle avoidance [11] and joint limit avoidance [12]) by using increased dexterity due to additional actuators. For example, a distributed actuation mechanism (DAM) [13], [14] was proposed to enhance fingertip force by relocating a redundant actuation position of a slider along a link without changing the posture. Any redundancy in a manipulator can be considered an additional design variable

The associate editor coordinating the review of this manuscript and approving it for publication was Guilin Yang.

(or freedom) to enhance the manipulation performance. However, the greater the redundancy of a manipulator, the greater the difficulty of precisely evaluating the maximum capability of a manipulator (velocity and force in this study).

As an alternative for redundancy resolution, gradient-based optimization has been successfully used in the fields [15], [16]. Gradient-based optimization is mathematical programming that can systematically and efficiently extremize an objective function (e.g., minimization of execution time, joint rotation, and travel length [17], and minimization of energy consumption, tracking error, and total weight of motors [18], minimization of sway of a robot body, forward movement error, and backward foot slipping [19], maximization of load carrying capacity [20], [21]) while satisfying the constraint functions (e.g., displacement, velocity, acceleration, and jerk of joints [22], the range of PD control gain values [23], and the rotation range of a superelastic flexure hinge [24]). An optimization-based method was also implemented to evaluate force capability for redundantly actuated parallel manipulators [25]. It is interesting to note that, in the field of structural analysis, the concept of allowable load set was introduced to define and visualize the set of loads that are structurally safe for a given working condition, using a gradient-based optimization [26].

In this study, a new concept of allowable velocity and force is proposed to precisely evaluate the maximum directional kinematic capability of a redundant manipulator in the task space. After the kinematic modeling of the manipulators (DAM-implemented three-link planar manipulator, 3RRR planar parallel manipulator (PPM), and UR5 selected for demonstration purposes) is derived for the end-effector velocity and force, gradient-based optimization is conducted to evaluate the maximum directional velocity and force at the end-effector projected along the given base direction. For validation, numerical simulation and experiments are conducted at several end-effector positions of the manipulator, thereby demonstrating the validity of the proposed method.

II. EVALUATION OF ALLOWABLE VELOCITY AND FORCE

A. LIMITATIONS OF MANIPULABILITY ELLIPSOID

For a general manipulator, the differential kinematic equation can be obtained as follows:

$$\mathbf{v}_e = \mathbf{J}(\boldsymbol{\theta})\dot{\boldsymbol{\theta}}, \tag{1}$$

where $\mathbf{v}_e$ is the end-effector velocity vector in the task space ($\mathbf{v}_e \in \mathbf{R}^m$), $\dot{\boldsymbol{\theta}}$ is the velocity vector in the joint space ($\dot{\boldsymbol{\theta}} \in \mathbf{R}^n$), and $\mathbf{J}(\theta)$ is the $m \times n$ Jacobian matrix with the components of $J_{ij} = \partial k_i(\theta)/\partial\theta_j$.

If the Euclidean norm of the joint-space velocity, which describes a unit sphere defined by

$$||\dot{\boldsymbol{\theta}}||^2 = \dot{\theta}_1^2 + \dot{\theta}_2^2 + \cdots + \dot{\theta}_n^2 \leq 1 \tag{2}$$

is considered, it is mapped into a velocity ellipsoid [1], [4]. This domain is defined by

$$\dot{\mathbf{x}}_e^{\mathrm{T}} \left(\mathbf{J}_p^{\mathrm{T}}\mathbf{J}_p\right) \dot{\mathbf{x}}_e \leq 1, \tag{3}$$

where $\mathbf{J}_p = \mathbf{J}^{\mathrm{T}}(\mathbf{J}\mathbf{J}^{\mathrm{T}})^{-1}$ denotes a pseudo inverse of $\mathbf{J}(\theta)$ for redundancy resolution.

In a similar way, a force ellipsoid can also be defined. Task-space forces are transformed into joint-space forces by using the same Jacobian matrix with the relation of

$$\boldsymbol{\tau} = \mathbf{J}^{\mathrm{T}}\mathbf{F}_e, \tag{4}$$

where $\boldsymbol{\tau}$ is the joint-space force vector and $\mathbf{F}_e$ is the task-space force vector at the end-effector. Then, one can consider the unit sphere of the joint-space forces as

$$||\boldsymbol{\tau}||^2 = \tau_1^2 + \tau_2^2 + \cdots + \tau_n^2 \leq 1, \tag{5}$$

and this is mapped into the task-space force ellipsoid, which is defined by

$$\mathbf{F}_e^{\mathrm{T}}\mathbf{J}\mathbf{J}^{\mathrm{T}}\mathbf{F}_e \leq 1. \tag{6}$$

The above approach of manipulability ellipsoid [2] has a severe limitation that maximum velocity and force estimated in the ellipsoids are not accurate because they are derived under the assumption that joint-space velocity and force form unit spheres with normalization [5], as expressed in Eq. (2). To overcome this limitation, the scaled velocity and force ellipsoid was derived using a scaling matrix with the limit values (i.e., upper or lower bound) of joint velocity and force [6], as follows:

$$\mathbf{v}^{\mathbf{T}}\mathbf{J}_p^{\mathbf{T}}\mathbf{W}_{\dot{\theta}}\mathbf{W}_{\dot{\theta}}\mathbf{J}_p\mathbf{v} = 1 \tag{7}$$

$$\mathbf{F}^{\mathrm{T}}\mathbf{J}\mathbf{W}_{\tau}\mathbf{W}_{\tau}\mathbf{J}^{\mathrm{T}}\mathbf{F} = 1 \tag{8}$$

where $\mathbf{W}_{\dot{\theta}} = \mathrm{diag}\left(1/\dot{\theta}_{1,\mathrm{lim}}, \cdots, 1/\dot{\theta}_{n,\mathrm{lim}}\right)$ and $\mathbf{W}_{\tau} = \mathrm{diag}\left(1/\tau_{1,\mathrm{lim}}, \cdots, 1/\tau_{n,\mathrm{lim}}\right)$. However, there still exists a problem that it is not possible to fully utilize (or consider) the joint-space velocity and/or force because actual joint space has a shape of a hypercube, not a sphere [5].

In addition, the manipulability ellipsoid cannot provide precise information on the maximum capability of a manipulator if the positional parameters (PPs)[1] such as link length and orientation angle significantly affect end-effector velocity and force. See footnote 1 for the terminology used in this study. For example, Fig. 1 shows a three-link planar manipulator in which link lengths are equal ($l_1 = l_2 = l_3 =$ 100mm). Note that, in Fig. 1, the position of the end effector is fixed at (0 mm, 150 mm), but the orientation of the end effector is not given. Therefore, θ_1 can be considered as the PP that can affect the end-effector velocity and force. As shown in Fig. 2(a), if the limit value of joint velocity is set at 0.2rad/s (i.e., $\max(\dot{\theta}_1) = \max(\dot{\theta}_2) = \max(\dot{\theta}_3) = 0.2$rad/s), the joint velocity space can be represented as a sphere. Using Eq. (7), scaled velocity ellipsoids can be obtained according to the value of θ_1 (Fig. 2(b)).

Conventional methods such as manipulability ellipsoid typically evaluate the maximum performance by considering

[1] In this study, among all control parameters (CPs), a positional parameter (PP) refers to the position and orientation which affect the performances of a manipulator, whereas a thrusting parameter (TP) refers to the speed and force used for the direct actuation control.

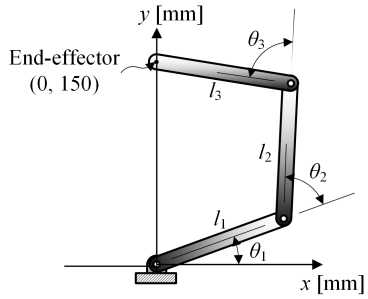

FIGURE 1. Three-link planar manipulator.

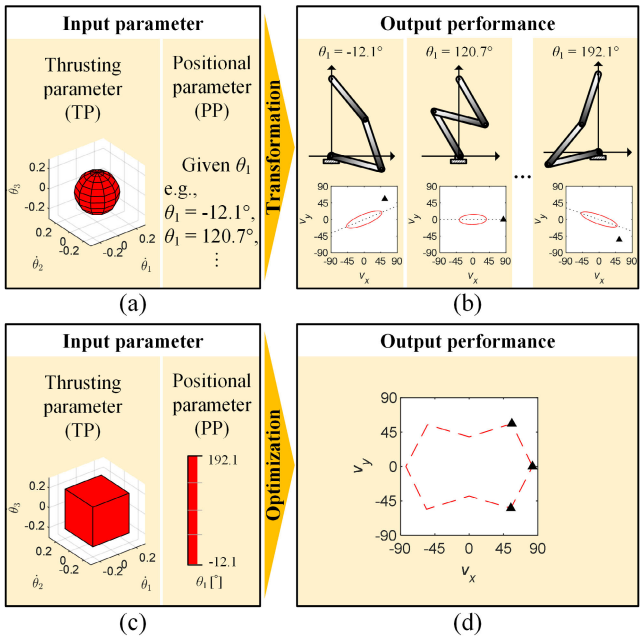

FIGURE 2. Comparison between the conventional and proposed method for a three-link planar manipulator: (a) spherical joint space velocity with a given joint angle θ_1, (b) velocity ellipsoid at $\theta_1 = -12.1°$, 120.7°, and 192.1° with the corresponding configurations of the manipulator, (c) cube-shaped joint space velocity with a variable joint angle θ_1, and (d) an allowable velocity polygon that visualizes the maximum velocities along the specific direction.

only the limited TPs at the joint space (i.e., a spherical shape in Fig. 2(a)) with given PPs. Therefore, the maximum performance of a redundant manipulator evaluated by manipulability ellipsoid significantly varies, depending on the PPs (e.g., first joint angle in Fig. 1). Its magnitude also shows a noticeable discrepancy due to the use of the limited TPs at the joint space, compared with a true value (black triangles in Fig. 2(b)). In addition, dotted lines when $\theta_1 = -12.1°$ and 192.1° in Fig. 2(b) represents the upper and lower boundaries of the major axis direction. Therefore, because the ellipsoids are determined by the transformation, there is a limit in the direction of the main axis.

Conversely, the proposed method can precisely evaluate the maximum performance by considering both a whole range of the TPs at the joint space (i.e., cubic shapes in Fig. 2(c)) and the PPs (a range from −12.1 to 192.1

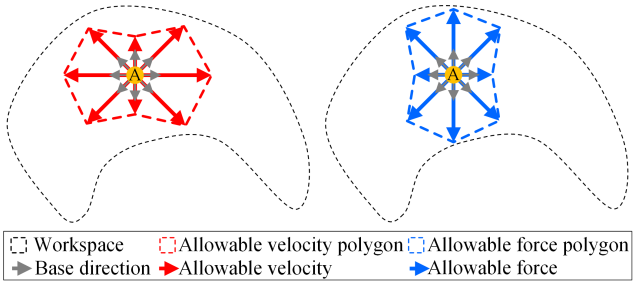

FIGURE 3. Concept of allowable velocity and force.

in Fig. 2(c)) at the same time. Note that the proposed method can simultaneously determine the optimized PPs and TPs as a result of optimization. Thus, these results indicate that the effect of the PPs on the manipulability ellipsoid needs to be thoroughly investigated for redundant manipulators.

In addition, the previous methods in the literature cannot provide quantitative information on maximum directional velocity and force projected on a given direction. Note that directional (or projected) performance should be carefully investigated for manipulators that operate on a *non-flat* surface because a task is typically given in a direction normal and/or tangential to the surface. Therefore, a new method needs to be developed to precisely evaluate the maximum directional performance of a manipulator along a particular direction and, at the same time, to determine the corresponding CPs for the optimal operation.

B. PROPOSED CONCEPT OF ALLOWABLE VELOCITY AND FORCE

In this study, the concept of allowable velocity and force is proposed to precisely evaluate the maximum directional performance of a manipulator projected along the given direction and to effectively visualize it in 2D and 3D.

For visualization of allowable velocity and force, a unit base direction (small gray arrows in Fig. 3) is selected at a target point in the workspace to represent the maximum directional velocity and force (red and blue arrows, respectively, in Fig. 3) projected along the same base direction. Connecting all the vertices of allowable velocity and force constructs allowable velocity and force polytopes, respectively. Note that the form of allowable velocity and force is a polygon in two-dimensional space and a polyhedron in three-dimensional space. Thus, these polytopes can effectively visualize allowable velocity and force in any arbitrary direction by interpolating the allowable velocity and force at two adjacent vertices.

In this study, gradient-based optimization was used to determine the maximum achievable values of end-effector velocity and force along each unit base direction. Note that gradient-based optimization has been widely used as a root-finding method for redundant problems in which the number of design variables is larger than the number of constraints [27]. Thus, the optimization can be formulated for a general manipulator, as follows:

i) Allowable velocity

$$\begin{aligned} &\text{Find} && \mathbf{z} \\ &\text{To maximize} && f_1(\mathbf{z}) = \mathbf{v}_e \cdot \mathbf{d}_i \quad i = 1, \cdots, M \\ &\text{Subject to} && g_1(\mathbf{z}) \le 0 \\ & && z_j^{(l)} \le z_j \le z_j^{(u)} \quad j = 1, \cdots, N \end{aligned} \tag{9}$$

ii) Allowable force

$$\begin{aligned} &\text{Find} && \mathbf{z} \\ &\text{To maximize} && f_2(\mathbf{z}) = \mathbf{F}_e \cdot \mathbf{d}_i \quad i = 1, \cdots, M \\ &\text{Subject to} && g_2(\mathbf{z}) \le 0 \\ & && z_j^{(l)} \le z_j \le z_j^{(u)} \quad j = 1, \cdots, N \end{aligned} \tag{10}$$

where the subscript i denotes the i-th unit base direction, and the superscripts (l) and (u) denote the lower and upper bounds, respectively. In Eqs. (9) and (10), $\mathbf{z}$ is an N-dimensional vector of the generalized design variables which represent the CPs to operate a manipulator. Objective functions (f_1 and f_2) indicate the end-effector velocity and force, respectively, projected along the unit base direction $\mathbf{d}_i$. The constraint functions (g_1 and g_2) are imposed to consider operating conditions such as limited power consumption. As a result of optimization, the optimized design variables ($\mathbf{z}$ in Eqs. (9) and (10)) can be determined and, at the same time, the corresponding allowable performance can also be obtained.

For example, assume two configurations of a three-link planar manipulator in Fig. 2(a). Then, for two different $\theta_1 = 190°$ and $20°$, the maximum values of conventional velocity ellipsoids are 51.5 mm/s and 41.3 mm/s (stars in the Fig. 2(c)), respectively. The corresponding orientations of major axes are $-19.0°$ and $27.4°$, respectively. However, the maximum values determined by the proposed allowable velocity are 86.4 mm/s and 67.8 mm/s (triangles in the Fig. 2(c)) along the corresponding base direction. Similarly, for $\theta_1 = 190°$ and $20°$, the maximum values of conventional force ellipsoid are 32.1 N and 18.2 N (stars in the Fig. 2(e)) along the major axes of $71.0°$ and $117.4°$, respectively. However, the maximum values determined by the proposed allowable force are 47.8 N and 45.5 N (triangles in the Fig. 2(e)) along the corresponding base directions. It should be emphasized that conventional manipulability ellipsoids cannot provide the exact maximum performance for redundant manipulators. Moreover, conventional manipulability ellipsoid cannot effectively visualize manipulation performance with a single diagram due to redundant PPs, as shown in Fig. 2.

III. EXAMPLES

To show the effectiveness and potential of the proposed method, the concept of allowable velocity and force was applied to three different types of manipulators: the DAM-implemented three-link planar manipulator (Fig. 4), 3RRR PPM (Fig. 10), and the UR5 which is a well-known 6-DOF spatial manipulator (Fig. 13). Those manipulators

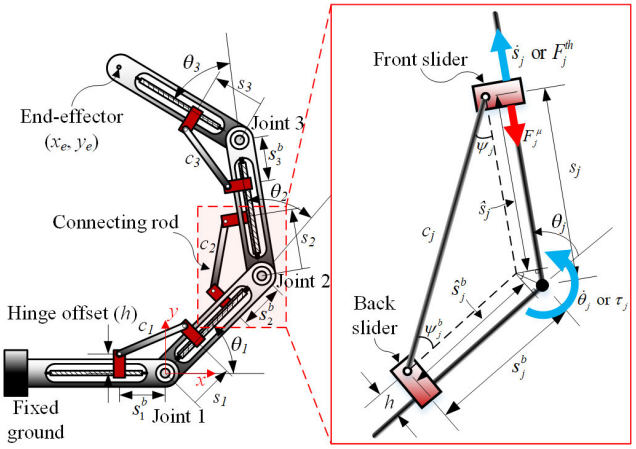

FIGURE 4. Three-link planar manipulator that equips distributed actuation mechanism.

investigated in this study can be kinematically redundant. DAM-based three-link planar manipulator becomes kinematically redundant when it is actuated by using three front sliders with no constraint on the orientation of the end-effector. Although UR5 is a non-redundant manipulator (six DOFs in both the joint and task space), it can be kinematically redundant for specific tasks such as simple end-effector positioning without any constraint on the orientation [15]. 3RRR PPM is also a non-redundant manipulator because three joints are actuated and the end-effector has three DOFs (x_e, y_e, ϕ in Fig. 10). However, if there exists no rotation restriction at the end-effector, it also becomes a kinematically redundant mechanism. Note that, in these redundant manipulators, end-effector performance is significantly affected by the PPs (e.g., position and angle) as well as the TPs (e.g., joint speed and force).

A. DAM-IMPLEMENTED THREE-LINK PLANAR MANIPULATOR

1) OPTIMIZATION RESULTS

The distributed actuation mechanism (DAM) is designed to generate a joint torque by thrusting a slider along a link instead of directly rotating a joint [13]. Consequently, the joint torque varies depending on the position of the slider, which is termed as the PP in this study. Controlling such redundant DOFs provide an additional design margin that can be used to enhance the end-effector performance at a target point [13], but makes it more difficult to precisely evaluate the maximum capability of the DAM. Fig. 4 shows a DAM-implemented three-link planar manipulator to be considered in this study. This manipulator has three joints, each of which consists of two sliders and one connecting rod. The end-effector velocity and force can be mathematically derived based on the following assumptions:

1) The end-effector position is given at (x_e, y_e);
2) Only front sliders are activated for manipulation. Therefore, the DAM has the same number of actuators as a typical three-link planar manipulator; and

3) Friction force can be expressed by the Coulomb friction model.

Considering the offset between a hinge joint and a slider (h in Fig. 4), the relation between the joint angle (θ_j) and the slider positions (s_j) can be expressed as follows:

$$c_j^2 = (\hat{s}_j)^2 + \left(\hat{s}_j^b\right)^2 + 2\,(\hat{s}_j)\left(\hat{s}_j^b\right)\cos\theta_j \quad \text{for } j = 1, 2, 3 \tag{11}$$

where $\hat{s}_j = s_j - h\tan(\theta_j/2)$; $\hat{s}_j^b = s_j^b - h\tan(\theta_j/2)$; $s_j^b = \sqrt{c_j^2 - \{(\hat{s}_j)\sin\theta_j\}^2} - (\hat{s}_j)\cos\theta_j + h\tan(\theta_j/2)$; c_j is the length of a connecting rod; h is the hinge offset; and s_j and s_j^b are the positions of the front and back sliders at the jth joint, respectively. Differentiating Eq. (11) with respect to time, the angular velocity of the jth joint can be obtained as follows:

$$\dot{\theta}_j = \frac{1}{D_j}\left\{\dot{s}_j\cos\theta_j\left(\hat{s}_j^b\right) + \dot{s}_j\,(\hat{s}_j)\right\} \quad \text{for } j = 1, 2, 3 \tag{12}$$

where $\dot{s}_j$ is the moving speed of the front sliders and $D_j = h\cos\theta_j(s_j + s_j^b) + \sin\theta_j(s_j s_j^b - h^2)$. Therefore, from Eq. (1), the end-effector velocity can be derived by combining Eq. (12) and 2×3 Jacobian matrix $\mathbf{J}$ for a general three-link planar manipulator [2]. In the previous study [13], the joint torque generated at the jth joint was derived as follows:

$$\tau_j = F_j^{th}\frac{s_j\tan\psi_j + h}{1 + \mu_j\tan\psi_j} \tag{13}$$

where $\psi_j = \cos^{-1}\left(c_j^2 + (\hat{s}_j)^2 - \left(\hat{s}_j^b\right)^2 / 2c_j\,(\hat{s}_j)\right)$; and F_j^{th} and μ_j are the thrusting force and the Coulomb friction coefficient at joint j, respectively. In this study, using the pseudo inverse method, the end-effector force is derived as follows:

$$\mathbf{F}_e = \left\{\left(\mathbf{J}\mathbf{J}^T\right)^{-1}\mathbf{J}\right\}\boldsymbol{\tau} \tag{14}$$

where $\boldsymbol{\tau} = \begin{bmatrix}\tau_1 & \tau_2 & \tau_3\end{bmatrix}^T$.

Based on the above mathematical derivation, optimization of the DAM-implemented three-link planar manipulator can be formulated as follows:

i) Allowable velocity

$$\begin{aligned}
&\text{Find} && \theta_1, \mathbf{s}, \text{ and } \dot{\mathbf{s}}\\
&\text{To maximize} && f_1(\theta_1, \mathbf{s}, \dot{\mathbf{s}}) = \mathbf{v}_e \cdot \mathbf{d}_i \quad i = 1, \cdots, M\\
&\text{Subject to} && g(\theta_1, \mathbf{s}, \dot{\mathbf{s}}) = \mathbf{F}_e \cdot \mathbf{v}_e \geq 0\\
&&& \theta_1^{(l)} \leq \theta_1 \leq \theta_1^{(u)}\\
&&& s_j^{(l)} \leq s_j \leq s_j^{(u)} \quad j = 1, 2, 3\\
&&& -\dot{s}_j^{(u)} \leq \dot{s}_j \leq \dot{s}_j^{(u)} \quad j = 1, 2, 3
\end{aligned} \tag{15}$$

ii) Allowable force

$$\begin{aligned}
&\text{Find} && \theta_1, \mathbf{s}, \text{ and } \mathbf{F}^{th}\\
&\text{To max}\,imize && f_2(\theta_1, \mathbf{s}, \mathbf{F}^{th}) = \mathbf{F}_e \cdot \mathbf{d}_i \quad i = 1, \cdots, M\\
&\text{Subject to} && g(\theta_1, \mathbf{s}, \mathbf{F}^{th}) = \mathbf{F}_e \cdot \mathbf{v}_e \geq 0\\
&&& \theta_1^{(l)} \leq \theta_1 \leq \theta_1^{(u)}
\end{aligned}$$

TABLE 1. Design parameters used for the DAM-implemented three-link planar manipulator.

Design variable	Joint 1		Joint 2		Joint 3	
	LB [a]	UB [b]	LB	UB	LB	UB
θ_1 [°]	$\theta_1^{(l)}$	$\theta_1^{(u)}$	$\theta_2^{(l)}$	$\theta_2^{(u)}$	$\theta_3^{(l)}$	$\theta_3^{(u)}$
s_j [mm]	37.0	77.0	37.0	77.0	37.0	77.0
F_j^{th} [N]	-56.0	56.0	-67.9	67.9	-56.3	56.3
$\dot{s}_j$ [mm]	-7.1	7.1	-6.9	6.9	-7.6	7.6

Design constant	Joint 1	Joint 2	Joint 3
l_j [mm]	114.0	114.0	129.0
c_j [mm]	80.0	80.0	80.0
μ_j	0.5	0.8	0.5
h [mm]		15.5	
M		16	

[a]LB: lower bound, [b]UB: upper bound

$$\begin{aligned}
&s_j^{(l)} \leq s_j \leq s_j^{(u)} \quad j = 1, 2, 3\\
&-F_j^{(u)} \leq F_j^{th} \leq F_j^{(u)} \quad j = 1, 2, 3.
\end{aligned} \tag{16}$$

Design variables for allowable velocity are the first joint angle (θ_1), the positions of the front slider (s_1, s_2, s_3), and the thrusting speeds of the front slider ($\dot{s}_1$, $\dot{s}_2$, $\dot{s}_3$); design variables for allowable force are the first joint angle (θ_1), the positions of the front slider (s_1, s_2, s_3), and the thrusting forces of the front slider (F_1^{th}, F_2^{th}, F_3^{th}). Note that the optimized design variables obtained from Eqs. (15) and (16) can be directly used as the CPs for the optimal operation of the manipulator. The superscripts (l) and (u) denote the lower and upper bounds of design variables to avoid singularity during operation. Then, the objective functions (f_1 and f_2) represent the end-effector velocity ($\mathbf{v}_e$) and the end-effector force ($\mathbf{F}_e$), respectively, projected along the unit base direction ($\mathbf{d}_i$). In Eq. (15), the end-effector velocity ($\mathbf{v}_e$) is composed of the joint thrusting velocity ($\dot{\theta}_i$) expressed in Eq. (12). Similarly, in Eq. (16), the end-effector force ($\mathbf{F}_e$) is composed of the joint thrusting torques (τ_i), which can be obtained using Eq. (13). The constraint function (g) imposes non-negative power consumption at the end effector for practical use. Design parameters used in the optimization are summarized in Table 1. In this study, a total of 16 base directions (i.e., $M = 16$ in Eq. (15) and (16)) were used to visualize allowable velocity and force for the planar mechanism, because it can precisely represent the manipulation performance. Sequential quadratic programming in MATLAB optimization toolbox [28] was used to solve Eqs. (15) and (16) as a well-proven gradient-based optimization algorithm.

The optimization results for allowable velocity and force at the end-effector position $(x, y) = (0\text{ mm}, 250\text{ mm})$ are shown in Fig. 5. It is interesting to note that conventional manipulability ellipsoid represents a simple elliptical shape (Fig. 2(c) and 1(e)), whereas the proposed method represents the polygons of a number-eight shape (Fig. 5(b) and 4(d)). As described in Section II.B, allowable velocity and force are

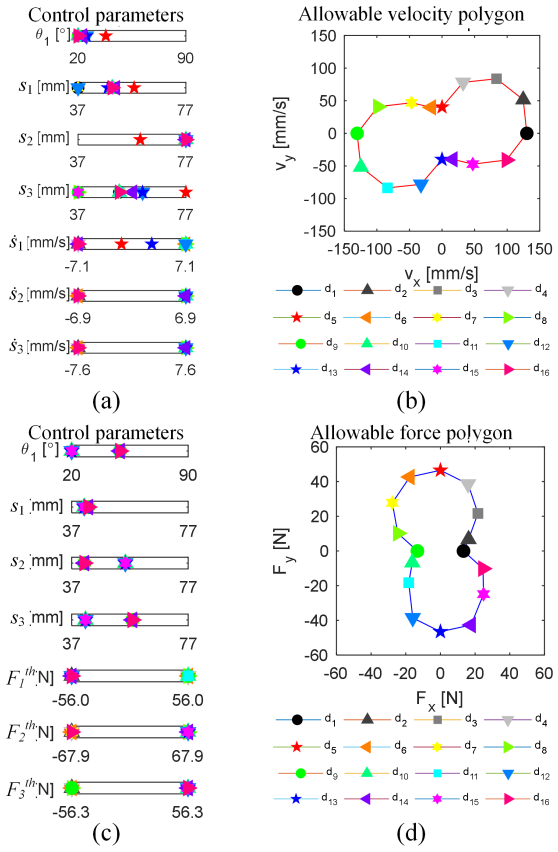

FIGURE 5. Optimization results for the DAM-implemented three-link planar manipulator at the end-effector position (x, y) = (0 mm, 250 mm) along a total of 16 base directions: (a) control parameters for allowable velocity, (b) allowable velocity polygons, (c) control parameters for allowable force, and (d) allowable force polygons.

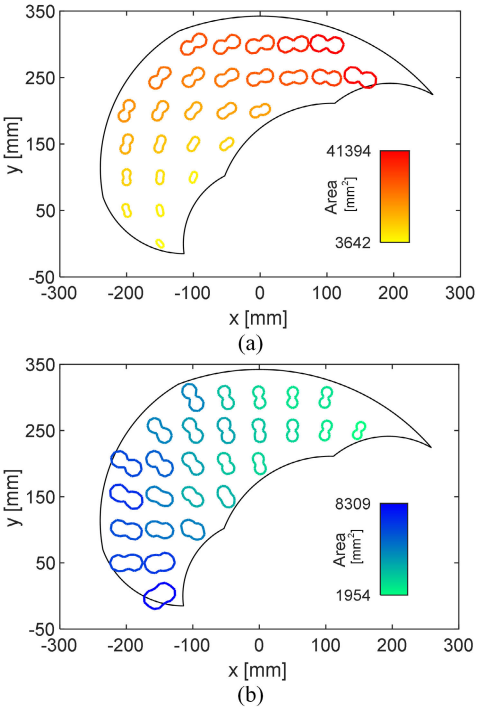

FIGURE 6. (a) Allowable velocity and (b) allowable force polygons in the workspace for the DAM-implemented three-link planar manipulator.

TABLE 2. Optimization results at the end-effector position (0 mm, 250 mm) along the base direction $\mathbf{d}_5 = (0, 1)$.

Design variables	Velocity mode		Force mode	
θ_1 [°]	38.0		20 [b]	
s_1 [mm]	57.8		41.3	
s_2 [mm]	60.1		55.4	
s_3 [mm]	77 [b]		41.7	
Thrusting parameters	$\dot{s}_1$ [mm/s]	-1.4	F_1^{th} [N]	56.0 [a]
	$\dot{s}_2$ [mm/s]	-6.9 [b]	F_2^{th} [N]	-67.9 [b]
	$\dot{s}_3$ [mm/s]	-7.6 [b]	F_3^{th} [N]	-56.3 [b]
Performance	**Velocity mode**		**Force mode**	
Velocity [mm/s]	40.3		28.9	
Force [N]	19.2		46.5	

[a]Upper bounded, [b]Lower bounded

obtained by maximizing the directional velocity and force projected onto each base direction and thereby determining the maximum directional performance. In principle, for maximization of the dot product between two vectors, it is necessary to increase the magnitude of vectors and/or to decrease a projection angle. Due to the above characteristic, several optimized design variables were not bounded (i.e., located at neither a lower nor upper bound), as shown in the Fig. 5(a) and 4(c). Thus, the optimal manipulator performance can be achieved although the CPs are not fully utilized. This is why conventional manipulability ellipsoid cannot precisely evaluate the maximum directional performance.

Figure 6 shows the allowable velocity and force of the DAM-implemented three-link planar manipulator at a total of 27 target positions, which are equidistantly distributed in the workspace. It is interesting to note that the major axes of the allowable velocity polygons (Fig. 6 (a)) tend to head in the tangential direction, whereas those of allowable force polygons (Fig. 6 (b)) are in the radial direction. In addition, the area of allowable velocity polygons tends to increase toward the right upper side, whereas that of allowable force polygons tends to increase toward the left lower side. These results originate from the kineto-statics duality between velocity and force, because they are obtained based on Eqs. (1) and (4), respectively [2]. Table 2 provides the detailed optimization results for allowable velocity and force at the end-effector position $(x, y) = (0\text{mm}, 250\text{mm})$ along the base direction $\mathbf{d}_5$. It should be noted that, $\dot{s}_1$ in the velocity mode is not bounded, but provides the maximum directional velocity.

To investigate the effectiveness of the proposed allowable (i.e., maximum directional) velocity and force, the "minimum" directional velocity and force were determined through the same optimization procedure except the minimization of the objective functions in Eqs. (15) and (16). For fair comparison, the same TPs that were determined in the maximum case were inputted to those in the minimum case,

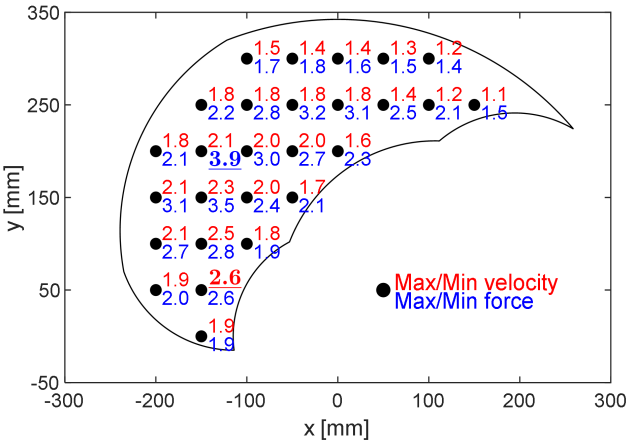

FIGURE 7. Comparison between the maximum and minimum directional performance with the same thrusting parameters for the DAM-implemented three-link planar manipulator (red: the maximum-to-minimum ratio for directional velocity, blue: the maximum-to-minimum ratio for directional force).

and then were set to be fixed during optimization. Therefore, only the PPs were used as design variables to investigate the variation of the manipulation performance.

Figure 7 shows the comparison between the maximum and minimum directional performances. Red and blue digits indicate the maximum-to-minimum area ratio of allowable velocity and force polygons, respectively, at a target position. The maximum area ratios of allowable velocity and force reach up to 2.6 and 3.9, respectively. It implies that, although the TPs were set to be the same, the manipulation performance in the maximum case is noticeably higher than that in the minimum case by simply allocating the slider positions and a joint angle at the corresponding optimal PPs.

2) EXPERIMENTAL VALIDATION

To validate the optimization results obtained in Section III.A.(1), a DAM-implemented three-link planar manipulator was manufactured, as presented in Fig. 8. For the sliding mechanism, three rotary geared motors (PGM, ϕ12) with a 1:16 gear reduction ratio were combined with lead screws and sliders. The total weight of the manipulator was 573.03 g; its size was 34 mm (H) × 43 mm (W) × 448 mm (L). To control the position of the slider, the Hall effect encoder embedded in each motor was utilized. The range of motion of the joint angles was from 0° to 90°. Specifications of the DAM-implemented three-link planar manipulator are described in Table 3. For validation, the end-effector velocity and force were measured at three target positions (-50 mm, 250 mm), (100 mm, 250 mm), and (-150 mm, 100 mm). The reference path of the sliders was generated using the optimization results determined in Section III.A.(1). The end-effector force was measured using a two-axis load cell at a 100 Hz sampling rate.

Comparison between the simulation and experimental results is shown in Fig. 9. The red and blue solid lines

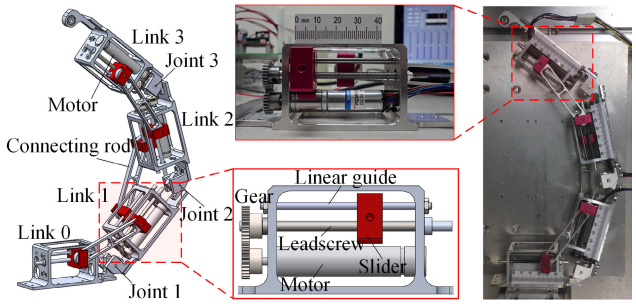

FIGURE 8. CAD model and the corresponding prototype of the DAM-implemented three-link planar manipulator.

TABLE 3. Specifications of the DAM-implemented three-link planar manipulator.

Items	Specifications
Total size [mm]	34 (H) × 43 (W) × 448 (L)
Total weight [g]	573.03
Actuator	DC motor (Motorbank Corp.)
Position sensor	Two channel hall effector encoder
Load cell	Tension and compression type (Bongshin Loadcell Corp.)

represent the allowable velocity and force polygons, respectively. The pink and light blue circles represent the velocity and force, respectively, experimentally measured at the target positions. The average errors between the simulated and measured data were 1.25% and 6.24% for the end-effector velocity and force, respectively.

B. 3RRR PLANAR PARALLEL MANIPULATOR

1) NUMERICAL RESULTS

A 3RRR PPM is a representative parallel robot with closed chains. Figure 10 shows a basic structure of the 3RRR PPM, in which the revolute joints are implemented and the three motors are equipped at A_1, A_2, and A_3. This manipulator consists of a kinematic chain with three closed loops ($A_1B_1C_1C_2B_2A_2$, $A_2B_2C_2C_3B_3A_3$, and $A_3B_3C_3C_1B_1A_1$ in Fig. 10), the end-effector (E) being rigidly attached to triangle $C_1C_2C_3$. It is assumed that the manipulator is symmetric with the same link length and the motors are located at the vertices (A_1, A_2, and A_3) which composes an equilateral triangle.

In [29], the velocity of the 3RRR PPM is expressed, as follows:

$$\mathbf{A}\mathbf{v}_e + \mathbf{B}\dot{\boldsymbol{\theta}} = 0 \tag{17}$$

where $\mathbf{v}_e = [\dot{x}_e,\ \dot{y}_e,\ \dot{\phi}]^{\mathrm{T}}$ and $\dot{\boldsymbol{\theta}} = [\dot{\theta}_1,\ \dot{\theta}_2,\ \dot{\theta}_3]^{\mathrm{T}}$. In Eq. (17), $\mathbf{A}$ and $\mathbf{B}$ are expressed as

$$\mathbf{A} = \begin{bmatrix} A_{11} & A_{12} & A_{13} \\ A_{21} & A_{22} & A_{23} \\ A_{31} & A_{32} & A_{33} \end{bmatrix},\quad \mathbf{B} = \begin{bmatrix} B_{11} & 0 & 0 \\ 0 & B_{22} & 0 \\ 0 & 0 & B_{33} \end{bmatrix} \tag{18}$$

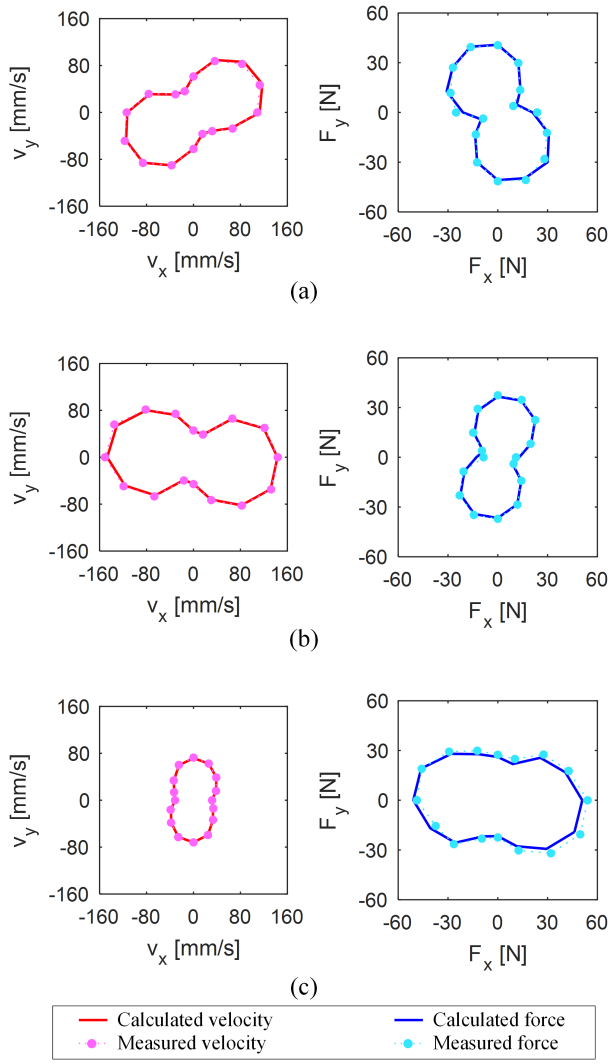

FIGURE 9. Comparison between the numerical and experimental results of allowable velocity and force for the DAM-implemented three-link planar manipulator: (a) at the position (−50 mm, 250 mm), (b) at the position (100 mm, 250 mm), and (c) at the position (−150 mm, 100 mm).

where the components A_{ij} and B_{ij} are given in [30].

For the 3RRR PPM, three distinct singularities occur in the configuration where either matrix **A** or **B** in Eq. (18) becomes singular. The first kind of singularity corresponds to the boundary of its workspace and occurs when the determinant of **B** vanishes. This is satisfied whenever link A_iB_i and link B_iC_i become aligned in a straight line. The second kind of singularity occurs when the determinant of **A** vanishes. This condition is satisfied when the extended lines along each of the three links, B_iC_i, intersect or when the three links, B_iC_i, are parallel. Third kind of singularity occurs when the determinants of both **A** and **B** vanish so that the first and second kind of singularities occur at the same time.

Considering the aforementioned singularities, the optimization for the 3RRR PPM can be formulated, as follows:

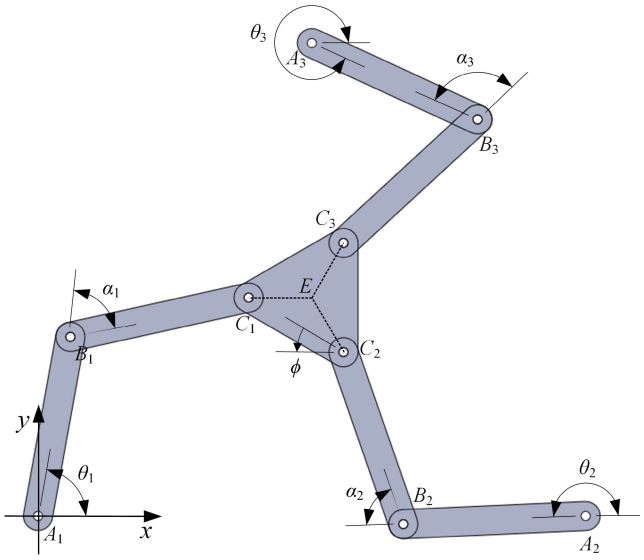

FIGURE 10. The 3RRR planar parallel manipulator.

i) Allowable velocity

$$\begin{aligned}
&\text{Find} && \dot{\theta}_1,\ \dot{\theta}_2,\ \dot{\theta}_3,\ \phi \\
&\text{To maximize} && f_1(\dot{\theta}_1,\ \dot{\theta}_2,\ \dot{\theta}_3,\ \phi) = \mathbf{v}_e^{\mathrm{T}} \cdot \mathbf{d}_i \quad i = 1, \cdots, N \\
&\text{Subject to} && g_1 = |\det(\mathbf{A})| \geq \varepsilon \\
& && g_2 = |\det(\mathbf{B})| \geq \varepsilon \\
& && \dot{\theta}_j^{(\mathrm{l})} \leq \dot{\theta}_j \leq \dot{\theta}_j^{(\mathrm{u})} \quad j = 1, \cdots, 3 \\
& && \phi^{(\mathrm{l})} \leq \phi \leq \phi^{(\mathrm{u})}
\end{aligned} \tag{19}$$

ii) Allowable force

$$\begin{aligned}
&\text{Find} && \tau_1,\ \tau_2,\ \tau_3,\ \phi \\
&\text{To maximize} && f_1(\tau_1,\ \tau_2,\ \tau_3,\ \phi) = \mathbf{v}_e^{\mathrm{T}} \cdot \mathbf{d}_i \quad i = 1, \cdots, N \\
&\text{Subject to} && g_1 = |\det(\mathbf{A})| \geq \varepsilon \\
& && g_2 = |\det(\mathbf{B})| \geq \varepsilon \\
& && \tau_j^{(\mathrm{l})} \leq \tau_j \leq \tau_j^{(\mathrm{u})} \quad j = 1, \cdots, 3 \\
& && \phi^{(\mathrm{l})} \leq \phi \leq \phi^{(\mathrm{u})}
\end{aligned} \tag{20}$$

where the subscript i denotes the ith base direction, and the superscripts (l) and (u) denote the lower and upper bounds, respectively, of design variables. In Eq. (19), design variables are the joint thrusting velocities ($\dot{\theta}_1,\ \dot{\theta}_2,\ \dot{\theta}_3$) and the orientation of the end-effector (ϕ) for the allowable velocity. Similarly, in Eq. (20), design variables are the joint thrusting torques ($\tau_1, \cdots, \tau_6$) and the orientation of the end-effector (ϕ) for the allowable force. The objective functions (f_1 and f_2) represent the end-effector velocity ($\mathbf{v}_e = [\dot{x}_e,\ \dot{y}_e,\ \dot{\phi}]^{\mathrm{T}}$) and the end-effector force ($\mathbf{F}_e = [F_x, F_y, \tau_z]$), respectively, projected along the unit base direction ($\mathbf{d}_i$). The constraint functions (g_1 and g_2) were imposed to avoid the first, second, and third kind of singularities. Design parameters for the simulation were selected from [31].

Figure 11 shows the optimization results for allowable velocity and force at a total of 15 target positions which are

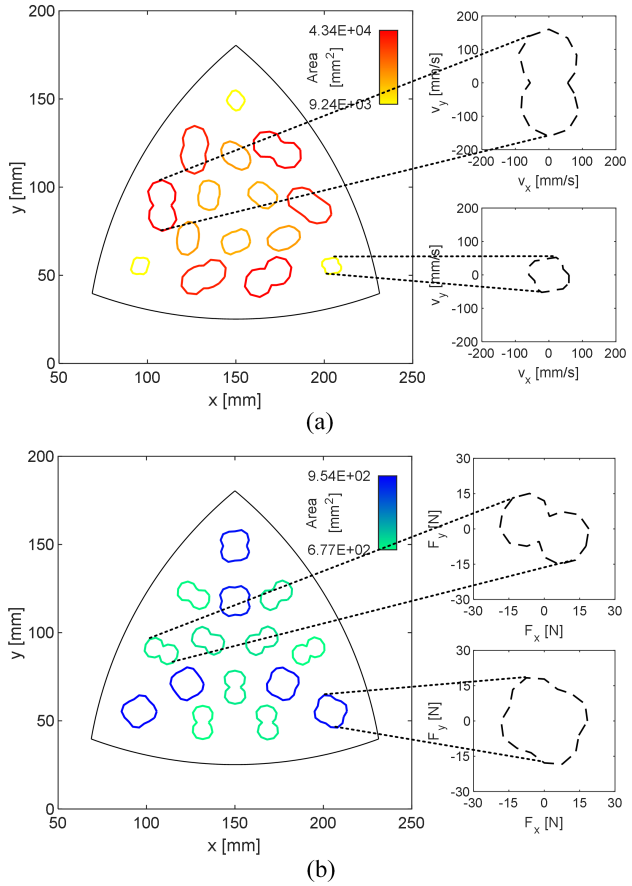

FIGURE 11. (a) Allowable velocity polygons and (b) allowable force polygons in the workspace for the 3RRR planar parallel manipulator.

equidistantly distributed in the workspace. The right side of Fig. 11(a) shows two allowable velocity polygons of different shapes at $\mathbf{p}_1 = (108.4\text{ mm}, 89.6\text{mm})$ and $\mathbf{p}_2 = (204.2\text{ mm}, 55.3\text{ mm})$. Note that these shapes cannot be determined by using conventional methods. The areas of allowable velocity polygons also have different values: 4.34E + 04 at $\mathbf{p}_1$ and 9.24E + 03 at $\mathbf{p}_2$. This indicates that the overall capability of end-effector velocity is greater at $\mathbf{p}_1$ than at $\mathbf{p}_2$. Similarly, the right side of Fig. 11(b) shows two allowable force polygons at $\mathbf{p}_1$ and $\mathbf{p}_2$, which shapes are not typical ellipses. The areas of allowable force polygons are 6.94E + 2 and 6.77E + 2 at $\mathbf{p}_1$ and $\mathbf{p}_2$, respectively. This implies that the overall capability of end-effector force is greater at $\mathbf{p}_1$ than at $\mathbf{p}_2$.

It is interesting to note that the major axes of the allowable velocity polygons for the 3RRR PPM tend to be in the tangential direction, whereas those of allowable force polygons are in the radial direction (Fig. 11). In addition, the color map for the polygon areas in Fig. 11(b) shows another tendency that the overall capability of end-effector velocity increases as the target point move away from the origin, whereas that of end-effector force generally increases as the target point move closer to the origin. These tendencies stem from the kineto-statics duality.

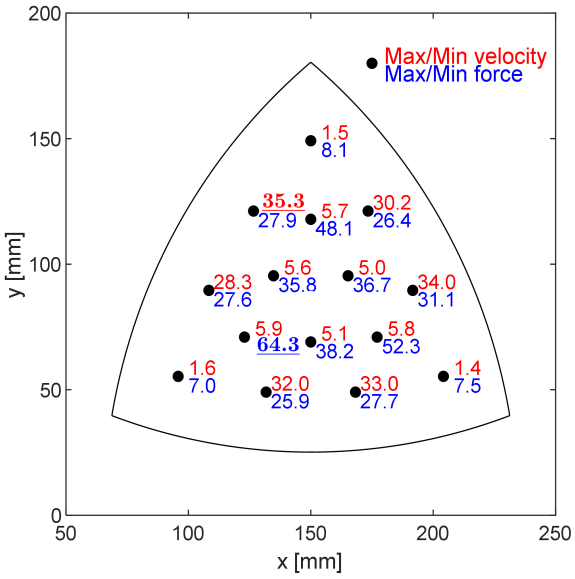

FIGURE 12. Comparison between the maximum and minimum achievable performances with the same thrusting parameters for the 3RRR planar parallel manipulator (red: the maximum-to-minimum ratio for directional velocity, blue: the maximum-to-minimum ratio for directional force).

Figure 12 shows a maximum-to-minimum area ratio of allowable velocity and force polygons for the 3RRR PPM. Although the TPs were set to be the same for fair comparison, overall performances can significantly vary depending on the PPs (e.g., orientation of the end effector). It shows that, although the TPs were set to be the same, the manipulation performance in the maximum case is noticeably higher than that in the minimum case due to the use of the optimal PPs.

2) VERIFICATION WITH COMMERCIAL MULTI-BODY DYNAMICS SOFTWARE

To check the validity of the allowable velocity and force of the 3RRR PPM, commercial multi-body dynamics software, RecurDyn, was used with an imported CAD model for the 3RRR PPM (Fig. 10). Using the same optimized TPs and PPs determined in the optimization, RecurDyn evaluated the end-effector velocity and force at a total of 15 target positions. The average errors of directional performance between the proposed method and RecurDyn were 7.96E-11% for allowable velocity and 2.15E-10% for allowable force. These errors can be considered negligible.

C. UR5 ROBOT

1) NUMERICAL RESULTS

The UR5 is a well-known 6-DOF spatial manipulator manufactured by Universal Robots [32]. In this study, the end-effector orientation angles (R, P, and Y) were selected as design variables, because the orientation of the end-effector was set to freely move at the given position. The joint angles ($\boldsymbol{\theta} = [\theta_1, \cdots, \theta_6]^{\mathrm{T}}$) of UR5 were determined using the inverse kinematics in [33]. A 6 × 6 Jacobian matrix $\mathbf{J}$ was

taken from [34]. Then, the end-effector velocity and force can be obtained using Eqs. (1) and (4), respectively.

Based on the aforementioned information, the optimization formulation for UR5 (Fig. 13) can be expressed, as follows:

i) Allowable velocity

$$\begin{aligned}
&\text{Find} && \dot{\boldsymbol{\theta}}, R, P, \text{ and } Y \\
&\text{To maximize} && f_1(\dot{\boldsymbol{\theta}}, R, P, Y) = \mathbf{v}_e^{\mathrm{T}} \cdot \mathbf{d}_i \quad i = 1, \cdots, M \\
&\text{Subject to} && g_1(\theta_3) = \sin^2\theta_3 - \sin^2(20^\circ) \geq 0 \\
& && g_2(\theta_5) = \sin^2\theta_5 - \sin^2(20^\circ) \geq 0 \\
& && g_3(\theta_2, \theta_3, \theta_4) = |G| > 0 \\
& && \dot{\theta}_j^{(l)} \leq \dot{\theta}_j \leq \dot{\theta}_j^{(u)} \quad j = 1, \cdots, 6 \\
& && 0 \leq R \leq 360^\circ \\
& && -90^\circ \leq P \leq 90^\circ \\
& && 0 \leq Y \leq 360^\circ
\end{aligned} \tag{21}$$

ii) Allowable force

$$\begin{aligned}
&\text{Find} && \boldsymbol{\tau}, R, P, \text{ and } Y \\
&\text{To maximize} && f_2(\boldsymbol{\tau}, R, P, Y) = \mathbf{F}_e^{\mathrm{T}} \cdot \mathbf{d}_i \;\; i = 1, \cdots, M \\
&\text{Subject to} && g_1(\theta_3) = \sin^2\theta_3 - \sin^2(20^\circ) \geq 0 \\
& && g_2(\theta_5) = \sin^2\theta_5 - \sin^2(20^\circ) \geq 0 \\
& && g_3(\theta_2, \theta_3, \theta_4) = |G| > 0 \\
& && \tau_j^{(l)} \leq \tau_j \leq \tau_j^{(u)} \;\; j = 1, \cdots, 6 \\
& && 0 \leq R \leq 360^\circ \\
& && -90^\circ \leq P \leq 90^\circ \\
& && 0 \leq Y \leq 360^\circ
\end{aligned} \tag{22}$$

where the subscript i denotes the i-th base direction; and the superscripts (l) and (u) denote the lower and upper bounds, respectively. In Eqs. (21) and (22), design variables are the joint thrusting velocities $(\dot{\theta}_1, \cdots, \dot{\theta}_6)$ and the RPY angles of the end-effector (R, P, Y) for the allowable velocity; the joint thrusting torques $(\tau_1, \cdots, \tau_3)$ and the RPY angles of the end-effector (R, P, Y) for the allowable force. The objective functions (f_1 and f_2) represent the end-effector velocity ($\mathbf{v}_e = [v_x, v_y, v_z, \omega_x, \omega_y, \omega_z]^{\mathrm{T}}$) and the end-effector force ($\mathbf{F}_e = [F_x, F_y, F_z, \tau_x, \tau_y, \tau_z]^{\mathrm{T}}$), respectively, projected along the unit base direction ($\mathbf{d}_i$). Because the UR5 operates in three-dimensional space, $\mathbf{d}_i$ can be expressed, as follows:

$$\mathbf{d}_i = [\sin\alpha\cos\beta,\ \sin\alpha\cos\beta,\ \cos\alpha]^{\mathrm{T}} \tag{23}$$

where α and β are polar and azimuth angles which ranges are $(0, \pi)$ and $(0, 2\pi)$, respectively (Fig. 13). By dividing these ranges into 45 degrees (not 22.5 degrees), a total of 26 base directions ($M = 26$ in Eqs. (21) and (22)) were selected to construct allowable velocity and force polyhedrons, efficiently. The singularity of the UR5 manipulator occurs when the determinant of the Jacobian matrix is 0, as follows:

$$\det(\mathbf{J}) = a_2 a_3 \sin\theta_3 \sin\theta_5 G = 0 \tag{24}$$

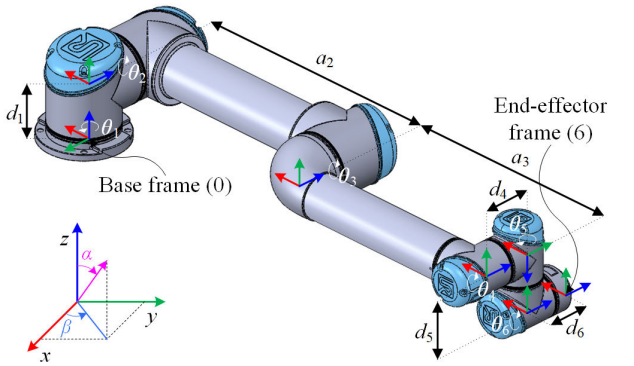

FIGURE 13. Coordinate systems and DH-parameters for the UR5 at a zero position.

where $G = a_2\cos\theta_2 + a_3\cos(\theta_2 + \theta_3) + d_5\sin(\theta_2 + \theta_3 + \theta_4)$. Therefore, the constraint functions (g_1, g_2, and g_3) were imposed to avoid this singularity. Design parameters (DH-parameters, joint speed, and torque limits) for the simulation were used from [32], [33].

Figure 14 shows the optimization results for allowable velocity and force for a total of 80 target positions equidistantly distributed in the workspace. The top of Fig. 14(a) shows two allowable velocity polyhedrons of different shapes at $\mathbf{p}_1$ = (200 mm, −200 mm, 289. 2 mm) and $\mathbf{p}_2$ = (−200 mm, −600 mm, 289.2 mm). Note that these shapes are not in a form of conventional manipulability ellipsoids. The volumes of allowable velocity polyhedrons (Vol in Fig. 14) also have different values: 44.3 and 136.4 for $\mathbf{p}_1$ and $\mathbf{p}_2$, respectively. This indicates that the overall capability of end-effector velocity is greater at $\mathbf{p}_2$ than at $\mathbf{p}_1$. The aspect ratios (AR in Fig. 14), which are defined as the ratio of the major axis to the minor axis, are 1.59 and 1.90 for $\mathbf{p}_1$ and $\mathbf{p}_2$, respectively. Because these polyhedrons are elongated in the direction of the major axis (0, 0, 1), the end-effector motion in this direction is faster than in other directions. Similarly, the top of Fig. 14(b) are allowable force polyhedrons at $\mathbf{p}_1$ and $\mathbf{p}_2$, which shapes are closer to a gourd bottle. The volumes of allowable force polyhedrons are 22.1 and 18.5 for $\mathbf{p}_1$ and $\mathbf{p}_2$, respectively. Contrary to the allowable velocity case, the overall capability of end-effector force is greater at $\mathbf{p}_1$ than $\mathbf{p}_2$. The aspect ratios are 2.34 and 3.21 for at $\mathbf{p}_1$ and $\mathbf{p}_2$, respectively, and two major axes are perpendicular to each other ((1, 0, 0) and (0, 1, 0) for $\mathbf{p}_1$ and $\mathbf{p}_2$, respectively).

Figure 14 clearly shows that the major axes of the allowable velocity polyhedrons for the UR5 tend to be in the tangential direction, whereas those of allowable force polyhedrons are in the radial direction (i.e., perpendicular to allowable velocity polyhedrons). The bottom of Fig. 14(a) and 10(b) shows the allowable velocity and force polygons, respectively, on planes Π_1, Π_2, and Π_3 at the position (200 mm, 200 mm, 289.2 mm). In addition, the color map for the polyhedron volume shows another tendency that the overall capability of end-effector velocity increases as the target point move away from the origin, whereas that of end-effector force increases as the target point move closer to the origin.

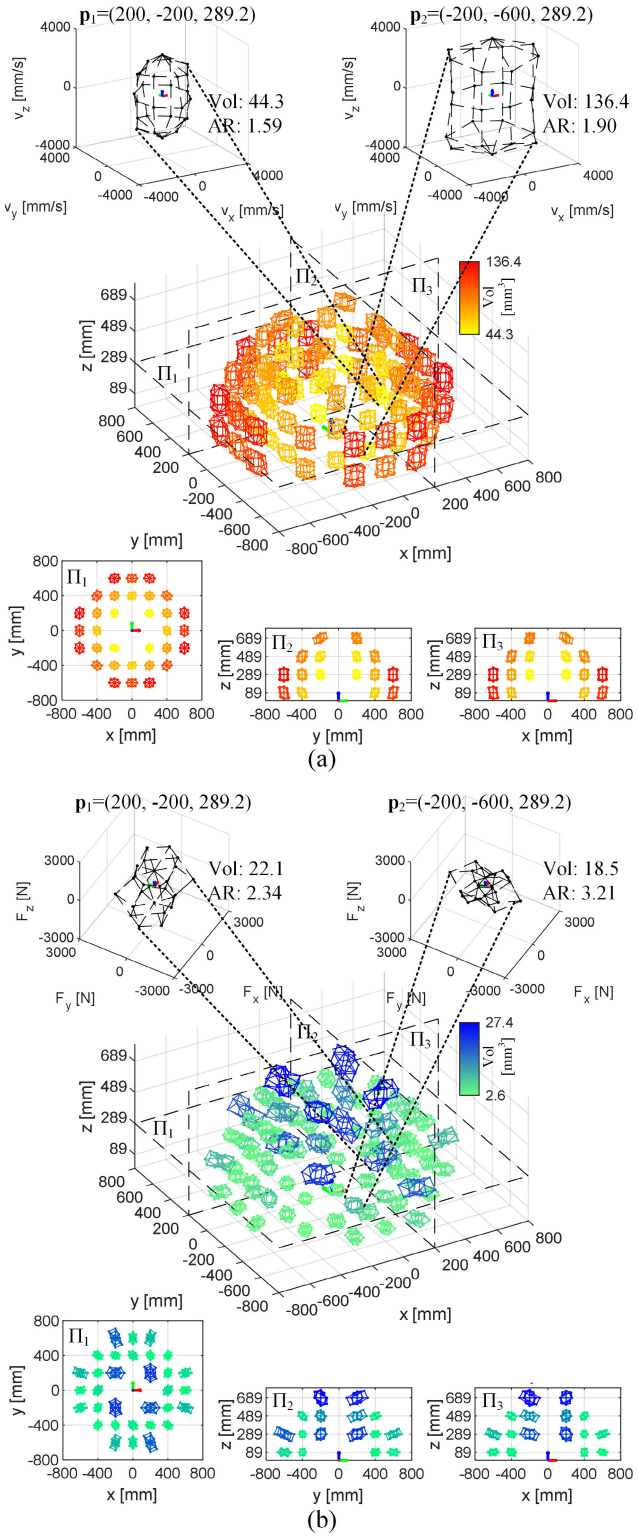

FIGURE 14. (a) Allowable velocity polyhedrons and (b) allowable force polyhedrons in the workspace for the UR5.

This tendency is similar with that of the DAM, also stemming from the kineto-statics duality.

Table 4 shows the allowable (i.e., maximum directional) velocity and the "minimum" directional velocity at $\mathbf{p}_1$ and $\mathbf{p}_2$

TABLE 4. Comparison between the maximum and minimum achievable velocity and force at the end-effector positions $\mathbf{p}_1$ = (200 mm, −200 mm, 289.2 mm) and $\mathbf{p}_2$ = (−200 mm, −600 mm, 289.2 mm) along the base direction with $\alpha = 45°$ and $\beta = 0°$ for the UR5.

Projected velocity						
Design variables	Lower bound	$\mathbf{p}_1$		$\mathbf{p}_2$		Upper bound
		Max	Min	Max	Min	
$\dot{\theta}_1$ [°/s]	-180	180	180	180	180	180
$\dot{\theta}_2$ [°/s]	-180	-180	-180	-180	-180	180
$\dot{\theta}_3$ [°/s]	-180	-180	-180	-180	-180	180
$\dot{\theta}_4$ [°/s]	-180	-180	-180	-180	-180	180
$\dot{\theta}_5$ [°/s]	-180	-180	-180	-180	-180	180
$\dot{\theta}_6$ [°/s]	-180	180	180	-180	-180	180
R [°]	0	45.6	216.3	17.7	163.4	360
P [°]	-90	-46.8	73.6	34.1	69.2	90
Y [°]	0	27.8	60.8	226.0	322.6	360
$\mathbf{v}_e \cdot \mathbf{d}$ [mm/s]	-	2609.9	1135.8	4229.9	3158.4	-
Max/Min	-	2.30		1.34		-
Projected force						
Design variables	Lower bound	$\mathbf{p}_1$		$\mathbf{p}_2$		Upper bound
		Max	Min	Max	Min	
τ_1 [Nm]	-150	150	150	150	150	150
τ_2 [Nm]	-150	-150	-150	-150	-150	150
τ_3 [Nm]	-150	-150	-150	150	150	150
τ_4 [Nm]	-28	28	28	28	28	28
τ_5 [Nm]	-28	-28	-28	-28	-28	28
τ_6 [Nm]	-28	-28	-28	-28	-28	28
R [°]	0	355.1	3.6	295.3	183.7	360
P [°]	-90	70.9	70.1	49.6	75.8	90
Y [°]	0	4.7	224.4	266.2	0.003	360
$\mathbf{F}_e \cdot \mathbf{d}$ [N]	-	2361.2	289.3	728.2	3.86e-09	-
Max/Min	-	8.16		1.89e+11		-

along the unit base direction with $\alpha = 45°$ and $\beta = 0°$. The minimum directional velocity was obtained to minimize the projected end-effector velocity with the same TPs determined in the maximum case. Although the TPs (i.e., joint speeds) were set to be the same in the maximum and minimum cases, the PPs (i.e., RPY angles) significantly affect the directional end-effector velocity of UR5. Such a wide variation in the directional performance (max/min ratios in Table 4) shows the importance of precisely evaluating the allowable performance by using the proposed method. Similarly, although the TPs (i.e., the joint torques) were set to be the same in the maximum and minimum cases, the PPs (i.e., RPY angles) significantly affect the directional end-effector force of the UR5.

Figure 15(a) and (b) show a maximum-to-minimum volume ratio of allowable velocity and force polyhedrons, respectively, for the UR5. Although the TPs were set to be the same for fair comparison, overall performances can significantly vary depending on the PPs (e.g., orientation of the end effector). As described in Section II.B, if the allowable

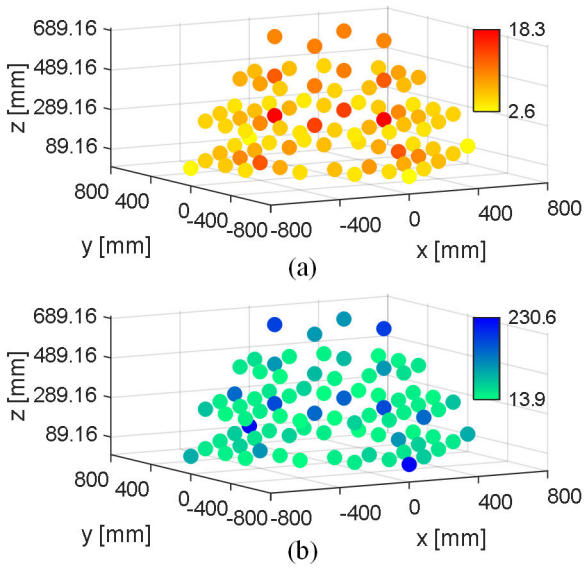

FIGURE 15. Comparison between the maximum and minimum achievable performances with the same thrusting parameters: (a) the maximum-to-minimum ratio for directional velocity and (b) the maximum-to-minimum ratio for directional force.

velocity and force polyhedrons are determined for a given manipulator, it is easy to estimate the maximum directional performance of the manipulator at a target position. Therefore, the proposed method can contribute to planning the optimal operation of a manipulator for a given task.

2) VERIFICATION WITH COMMERCIAL MULTI-BODY DYNAMICS SOFTWARE

To check the validity of the allowable velocity and force of the UR5 manipulator, commercial multi-body dynamics software, RecurDyn, was used with an imported CAD model for the UR5 (Fig. 13). Using the same optimized TPs and PPs determined in Section III.C.(1), RecurDyn evaluated the end-effector velocity and force at $\mathbf{p}_3 = (200\text{ mm}, 400\text{ mm}, 89.2\text{ mm})$ and $\mathbf{p}_4 = (400\text{ mm}, 400\text{ mm}, 289.2\text{ mm})$. The average errors of directional performance between the proposed method and RecurDyn were 0.27% and 0.46% at $\mathbf{p}_3$ and $\mathbf{p}_4$, respectively, for allowable velocity; 1.13% and 1.55% at $\mathbf{p}_3$ and $\mathbf{p}_4$, respectively, for allowable force. These errors, albeit negligible, mainly stem from numerical errors such as truncation and manipulation errors.

IV. CONCLUSION

Based on a new concept of allowable velocity and force, this study proposed a novel optimization-based method that can precisely determine the maximum directional kinematic capability of a redundant manipulator projected along a specific direction. Unlike conventional manipulability ellipsoid, the proposed method can provide reliable information on the maximum directional velocity and force with more effective visualization. The optimized CPs (i.e., PPs and TPs), which are also obtained by the proposed method, can be directly embedded in the manipulator for the optimal operation. The numerical and experimental results for the DAM-implemented three-link planar manipulator and the UR5 manipulator demonstrate the advantages and potential of the proposed method. Thus, the proposed method would contribute to planning the optimal operation for an assigned complicated task by fully utilizing the limited resources of a redundant manipulator.

V. ACKNOWLEDGMENT

(Jong Ho Kim and Young June Shin are co-first authors.)

REFERENCES

[1] T. Yoshikawa, "Manipulability of robotic mechanisms," *Int. J. Robot. Res.*, vol. 4, no. 2, pp. 3–9, Jun. 1985.
[2] B. Siciliano, L. Sciavicco, L. Villani, and G. Oriolo, *Robotics: Modelling, Planning and Control*. London, U.K.: Springer, 2009.
[3] T. Yoshikawa, *Foundations of Robotics: Analysis and Control*. Cambridge, MA, USA: MIT Press, 1990.
[4] S. L. Chiu, "Task compatibility of manipulator postures," *Int. J. Robot. Res.*, vol. 7, no. 5, pp. 13–21, Oct. 1988.
[5] R. Finotello, T. Grasso, G. Rossi, and A. Terribile, "Computation of kinetostatic performances of robot manipulators with polytopes," in *Proc. IEEE Int. Conf. Robot. Automat.*, vol. 4, May 1998, pp. 3241–3246.
[6] P. Chiacchio, Y. Bouffard-Vercelli, and F. Pierrot, "Force polytope and force ellipsoid for redundant manipulators," *J. Robotic Syst.*, vol. 14, no. 8, pp. 613–620, Aug. 1997.
[7] T. Takaki and T. Omata, "High-performance anthropomorphic robot hand with grasping-force-magnification mechanism," *IEEE/ASME Trans. Mechatronics*, vol. 16, no. 3, pp. 583–591, Jun. 2011.
[8] T. Takayama, T. Yamana, and T. Omata, "Three-fingered eight-DOF hand that exerts 100-N grasping force with force-magnification drive," *IEEE/ASME Trans. Mechatronics*, vol. 17, no. 2, pp. 218–227, Apr. 2012.
[9] Y. J. Shin, H. J. Lee, K.-S. Kim, and S. Kim, "A robot finger design using a dual-mode twisting mechanism to achieve high-speed motion and large grasping force," *IEEE Trans. Robot.*, vol. 28, no. 6, pp. 1398–1405, Dec. 2012.
[10] S. H. Jeong, Y. J. Shin, and K.-S. Kim, "Design and analysis of the active dual-mode twisting actuation mechanism," *IEEE/ASME Trans. Mechatronics*, vol. 22, no. 6, pp. 2790–2801, Dec. 2017.
[11] G. S. Chyan and S. G. Ponnambalam, "Obstacle avoidance control of redundant robots using variants of particle swarm optimization," *Robot. Comput.-Integr. Manuf.*, vol. 28, no. 2, pp. 147–153, Sep. 2011.
[12] D. Omrčen, L. Žlajpah, and B. Nemec, "Compensation of velocity and/or acceleration joint saturation applied to redundant manipulator," *Robot. Auto. Syst.*, vol. 55, no. 4, pp. 337–344, Apr. 2007.
[13] Y. J. Shin and K.-S. Kim, "Distributed-actuation mechanism for a finger-type manipulator: Theory and experiments," *IEEE Trans. Robot.*, vol. 26, no. 3, pp. 569–575, Jun. 2010.
[14] J. H. Kim, Y. J. Shin, S. Kim, and I. G. Jang, "Dual-mode operation of the finger-type manipulator based on distributed actuation mechanism," in *Proc. 11th World Congr. Struct. Multidisciplinary Optim.*, 2015, pp. 1–6.
[15] S. Chiaverini, G. Oriolo, and A. A. Maciejewski, "Redundant robots," in *Handbook of Robotics*. Cham, Switzerland: Springer, 2016, pp. 221–242.
[16] M. Faroni, M. Beschi, N. Pedrocchi, and A. Visioli, "Predictive inverse kinematics for redundant manipulators with task scaling and kinematic constraints," *IEEE Trans. Robot.*, vol. 35, no. 1, pp. 278–285, Feb. 2019.
[17] L. Wang, Q. Wu, F. Lin, S. Li, and D. Chen, "A new trajectory-planning beetle swarm optimization algorithm for trajectory planning of robot manipulators," *IEEE Access*, vol. 7, pp. 154331–154345, 2019.
[18] E. A. Padilla-Garcia, A. Rodriguez-Angeles, J. R. Resendiz, and C. A. Cruz-Villar, "Concurrent optimization for selection and control of AC servomotors on the powertrain of industrial robots," *IEEE Access*, vol. 6, pp. 27923–27938, 2018.
[19] J. H. Lee and J. H. Park, "Optimization of postural transition scheme for quadruped robots trotting on various surfaces," *IEEE Access*, vol. 7, pp. 168126–168140, 2019.

[20] M. H. Korayem, V. Azimirad, A. Nikoobin, and Z. Boroujeni, "Maximum load-carrying capacity of autonomous mobile manipulator in an environment with obstacle considering tip over stability," *Int. J. Adv. Manuf. Technol.*, vol. 46, nos. 5–8, pp. 811–829, Jan. 2010.
[21] M. H. Korayem and H. Tourajizadeh, "Maximum DLCC of spatial cable robot for a predefined trajectory within the workspace using closed loop optimal control approach," *J. Intell. Robotic Syst.*, vol. 63, no. 1, pp. 75–99, Jul. 2011.
[22] J. Ogbemhe, K. Mpofu, and N. Tlale, "Optimal trajectory scheme for robotic welding along complex joints using a hybrid multi-objective genetic algorithm," *IEEE Access*, vol. 7, pp. 158753–158769, 2019.
[23] V. Prada-Jimenez, P. A. Nino-Suarez, E. A. Portilla-Flores, and M. F. Mauledoux-Monroy, "Tuning a PD+ controller by means of dynamic optimization in a mobile manipulator with coupled dynamics," *IEEE Access*, vol. 7, pp. 124712–124726, 2019.
[24] M. Yang, C. Zhang, G. Yang, and W. Dong, "Optimal design and tracking control of a superelastic flexure hinge based 3-PRR compliant parallel manipulator," *IEEE Access*, vol. 7, pp. 174236–174247, 2019.
[25] S. B. Nokleby, R. Fisher, R. P. Podhorodeski, and F. Firmani, "Force capabilities of redundantly-actuated parallel manipulators," *Mech. Mach. Theory*, vol. 40, no. 5, pp. 578–599, May 2005.
[26] B. M. Kwak and J. H. Kim, "Concept of allowable load set and its application for evaluation of structural integrity," *Mech. Struct. Mach.*, vol. 30, no. 2, pp. 213–247, Jan. 2002.
[27] J. Arora, *Introduction to Optimum Design*. New York, NY, USA: Academic, 2004.
[28] M. A. Branch and A. Grace, *Optimization Toolbox: For use With MATLAB: User's Guide: Version 1*. Natick, MA, USA: Math works, 1998.
[29] C. Gosselin and J. Angeles, "Singularity analysis of closed-loop kinematic chains," *IEEE Trans. Robot. Autom.*, vol. 6, no. 3, pp. 281–290, Jun. 1990.
[30] J. Wu, J. Wang, L. Wang, and Z. You, "Performance comparison of three planar 3-DOF parallel manipulators with 4-RRR, 3-RRR and 2-RRR structures," *Mechatronics*, vol. 20, no. 4, pp. 510–517, Jun. 2010.
[31] S. Kucuk, "Energy minimization for 3-RRR fully planar parallel manipulator using particle swarm optimization," *Mech. Mach. Theory*, vol. 62, pp. 129–149, Apr. 2013.
[32] Universal Robots. (2019). *UNIVERSAL ROBOT UR5*. Accessed: Mar. 10, 2020. [Online]. Available: https://www.universal-robots.com/products/ur5-robot/
[33] P. M. Kebria, S. Al-wais, H. Abdi, and S. Nahavandi, "Kinematic and dynamic modelling of UR5 manipulator," in *Proc. IEEE Int. Conf. Syst., Man, Cybern. (SMC)*, Oct. 2016, pp. 004229–004234.
[34] A. Østvik, "Robot control in image-guided intervention," M.S. thesis, Dept. Phys., Norwegian Univ. Sci. Technol., Trondheim, Norway, 2016.

JONG HO KIM received the B.S. degree from the Department of Mechanical Engineering, Inha University, Incheon, South Korea, in 2013, and the M.S. and Ph.D. degrees from the Cho Chun Shik Graduate School of Green Transportation, Korea Advanced Institute of Science and Technology (KAIST), Daejeon, South Korea, in 2015 and 2021, respectively.

His research interest includes the efficient actuating mechanism of robot system using optimization scheme.

YOUNG JUNE SHIN received the B.S. degree from Korea Aerospace University, in 2007, and the M.S. and Ph.D. degrees from the Department of Mechanical Engineering, Korea Advanced Institute of Science and Technology (KAIST), in 2009 and 2013, respectively.

He is currently a Senior Researcher with Agency for Defense Development, Daejeon, South Korea. His current research interests include design and control of wearable robots.

IN GWUN JANG (Member, IEEE) received the B.S. and Ph.D. degrees from the Department of Mechanical Engineering, Korea Advanced Institute of Science and Technology (KAIST), Daejeon, South Korea, in 1999 and 2006, respectively.

He is currently an Associate Professor with the Cho Chun Shik Graduate School of Green Transportation, KAIST. He worked at Queens University, Kingston, Canada, as a Postdoctoral Fellow. His expertise covers design optimization ranging from the component-level to system-level, based on computational analysis. His current research interest includes to develop a new actuation mechanism which can maximize the manipulation performance for a given task.